

# Segmentation of Retinal Blood Vessels by Combining the Detection of Centerlines and Morphological Reconstruction

Ana Maria Mendonça, *Senior Member, IEEE*, and Aurélio Campilho, *Member, IEEE*

**Abstract**—This paper presents an **automated** method for the segmentation of the vascular network in retinal images. The algorithm starts with the **extraction of vessel centerlines**, which are used as guidelines for the subsequent vessel filling phase. For this purpose, the outputs of four directional differential operators are processed in order to select connected sets of candidate points to be further classified as centerline pixels using vessel derived features. **The final segmentation is obtained using an iterative region growing method** that integrates the contents of several binary images resulting from vessel width dependent morphological filters. Our approach was tested on two publicly available databases and its results are compared with recently published methods. The results demonstrate that our algorithm outperforms other solutions and approximates the **average accuracy of a human observer** without a significant degradation of sensitivity and specificity.

**Index Terms**—Edge detection, morphological processing, ophthalmology, retinal images, vessel segmentation.

## I. INTRODUCTION

**T**HE quantification of vessel features, such as length, width, tortuosity and branching pattern, among others, can provide new insights to diagnose and stage pathologies which affect the morphological and functional characteristics of blood vessels. However, when the vascular network is complex, or the number of images is large, manual measurements can become tiresome or even impossible. **A feasible solution is the use of automated analysis, which is nowadays commonly accepted by the medical community.**

Retinal images are influenced by all the factors that affect the body vasculature in general. Moreover the eye is the very unique region of the human body where the vascular condition can be directly observed *in vivo*. Along with the fovea and optic disc, the vascular tree constitutes one of the main features of an ocular fundus image and several of its properties are noticeably affected by worldwide major diseases such as diabetes, hypertension, and arteriosclerosis. Other eye diseases, such as choroidal

neovascularization [1] and retinal artery occlusion [2], also induce changes in the retinal vasculature. For the reasons here stated, the segmentation of retinal images can be a valuable aid for the detection and follow-up of several pathological states, as a mean of detecting and characterizing over time any of the changes in the blood vessels.

Some of the main clinical objectives reported in the literature for retinal vessel segmentation are the implementation of screening programs for diabetic retinopathy [3]–[5], evaluation of the retinopathy of prematurity [6], macular avascular region detection [7], arteriolar narrowing [8], [9], vessel tortuosity to characterize hypertensive retinopathy [10], vessel diameter measurement to diagnose hypertension, and cardiovascular diseases [11]–[13], and computer-assisted laser surgery [1], [14]. Other indirect applications include automatic generation of retinal maps for the treatment of age-related macular degeneration [15], extraction of characteristic points of the retinal vasculature for temporal or multimodal image registration [16]–[18], retinal image mosaic synthesis [19], identification of the optic disc position [20], [21], and localization of the fovea [22]. Furthermore, the network of retinal vessels is distinctive enough to each individual and can be used for biometric identification, although it has not yet been extensively explored [19].

In this paper, we present an algorithm for the automated detection of the retinal vascular network which **combines differential filters, for centerline extraction, with morphological operators, used for filling vessel segments.** Several intensity and morphological properties of vascular structures, such as linearity, connectivity, and width, are considered in our approach. **The segmentation of blood vessels herein described has the following main phases:** 1) image preprocessing for background normalization and thin vessel enhancement; 2) vessel centerline detection for defining a set of points in the central part of the vessels; 3) seeded region growing, to fill finally the blood vessels. **Vessel centerlines**, considered as local intensity maxima along vessel cross profiles, are detected using the signs of four directional operators. These centerline segments are the seeds for an iterative region growing process, which in each step uses one level of a multiscale representation of the vascular structure based on a morphological approach with variable sized structuring elements.

The method was evaluated using the images of two publicly available databases, the DRIVE database [5] and the STARE database [23]. The results of this work are compared with those from other recent methods, leading to the conclusion that our algorithm outperforms other solutions, while approximating

Manuscript received December 12, 2005; revised May 17, 2006. Asterisk indicates corresponding author.

\*A. M. Mendonça is with the Signal and Image Laboratory, Institute for Biomedical Engineering, and also with the Department of Electrical and Computer Engineering, University of Porto, Campus da FEUP/DEEC, 4200-465 Porto, Portugal (e-mail: amendon@fe.up.pt).

A. Campilho is with the Signal and Image Laboratory, Institute for Biomedical Engineering, and also with the Department of Electrical and Computer Engineering, University of Porto, Campus da FEUP/DEEC, 4200-465 Porto, Portugal (e-mail: campilho@fe.up.pt).

Digital Object Identifier 10.1109/TMI.2006.879955

the average accuracy of a human observer without a significant degradation of sensitivity and specificity.

The paper is organized as follows. In Section II, some of the methods previously presented for retinal vessel segmentation are briefly mentioned. Section III contains an overview of our proposal for retinal vessel segmentation. A method for the extraction of vessel centerlines is proposed in Section IV, and the vessel segmentation algorithm is described in Section V. The results of the tests on the images of the DRIVE and STARE databases are presented in Section VI, where a comparison with other solutions can also be found. Finally, Section VII is devoted to the discussion and presentation of the main conclusions of this work.

## II. METHODS FOR RETINAL VESSEL SEGMENTATION

The methods used for identifying vessels in two-dimensional (2-D) images are generally based on local image features, taking into account the specific properties of the vascular segments. Two main approaches are normally considered for the identification of general vascular segments [24], associated with two different strategies for classifying each pixel as belonging to a vessel or not. These two categories are also found in retinal vasculature segmentation applications [19], where the algorithms for detecting blood vessels are generally grouped as *pixel processing-based* methods and *tracking* methods. The former class is divided by some authors in *kernel-based* and *classifier-based* methods [25]. Other classification schemes are proposed in the literature, as the division into *rule-based* methods and *supervised* methods mentioned in [5].

*Pixel processing-based* methods frequently use a two-step approach. The first step is an enhancement procedure, usually a convolution operator, with the main purpose of selecting an initial set of pixels to be further validated as vessels in the second step. The emphasis given to each one of these two phases justifies the subdivision proposed in [25]. Several distinctive solutions are described in the literature for *pixel processing-based* methods. The concept of matched filter detection was proposed by Chaudhuri *et al.* in [26]. In this method, the authors use 12 rotated versions of a 2-D Gaussian shaped template for searching vessel segments along all possible directions. For every pixel, the maximum response to these kernels is retained. As each convolution kernel is modified by subtracting its mean value, the expected filter output is ideally zero in the background, and the resulting image can be easily thresholded to produce a binary representation of the retinal vasculature. Other matched filtering approaches using global [27] or local thresholding strategies [23] have been reported for the segmentation of retinal vessels. Differential filters, based either on first- or second-order derivatives, can be used for vessel borders extraction. In [15], the edge information is combined to identify candidates for vessel cross sections, producing subsequently the final centerline segments. Martinez-Perez *et al.* proposed a method where features derived from image derivatives obtained at multiple scales are used in a two-stage region growing procedure which segments progressively the retinal vessels [28], [29]. The combination of edge detection, matched filtering, and region growing is presented in [30] as a fast solution for automated detection of retinal blood

vessels. The use of a 2-D wavelet transform for the segmentation of the vessels in fundus images is reported in [4]. In [25], vessel detection is achieved by thresholding, after the convolution of the image with a 2-D Laplacian kernel. A general framework of adaptive local thresholding based on the use of a multi-threshold scheme, combined with a classification procedure to verify each resulting binary object, was presented by Jiang *et al.* in [31]; the incorporation of relevant information related with retinal vessels in the classification process allows the application of this generic methodology to images of the retina. In [32], Zana *et al.* proposed an algorithm that combines morphological filters and cross-curvature evaluation to segment vessel-like patterns in retinal images; in this method, the use of morphological filters leads to a simplified image where the computation of cross-curvatures is easy, since vessel segments are considered as the only image features whose curvature is linearly coherent. Another mathematical morphology approach to retinal vessel segmentation, which uses the top-hat transform calculated from the supremum of openings with large linear structuring elements in different directions, is described in [33]. Niemeijer *et al.* presented a vessel segmentation algorithm based on pixel classification using a simple feature vector [34]. For each pixel, features are extracted from the green-channel image, and a K-nearest neighbor (kNN) classifier outputs a soft classification that indicates the probability of being a vessel point. Another supervised method, called primitive-based method, was proposed by Staal *et al.* in [5]; this algorithm is based on the extraction of ridges, used as primitives for describing linear segments, named line elements; each pixel, which is assigned to the nearest line element to form image patches, is classified using a set of features from the corresponding line and image patch. In [35], retinal vessels are identified using a neural network whose inputs are derived from principal component analysis of the image and edge detection of the first principal component.

*Tracking* methods start by locating, manually or automatically, the vessel points used for tracing the vasculature, by measuring some local image properties. These methods, that only evaluate the pixels close to the initial positions, are also mentioned as exploratory algorithms. The algorithms are normally implemented as a single-pass operation, where the extraction of image features and the recognition of the vessel structure are simultaneously executed. Most of the methods reported in the literature use Gaussian functions to characterize the vessel profile. In [2], the authors report an algorithm that is initiated by the definition of the starting and ending points and is automatically followed by a matched filter for locating the vessel boundaries, tracking the midline and extracting parameters of clinical interest. This methodology is extended in [36] with the objective of detecting the end of the vessels, and successfully tracking down new vessels at bifurcations. To deal with the problem of the central light reflex area, in [11] vessel intensity profiles are modeled using twin Gaussian functions. In [37], the tracking process begins from the circumference of the optic disc, being a Kalman filter the base to estimate the next search location. The method proposed in [38] also overcomes the problem of initialization, but does not require vessel profile modeling; initial points are detected on the bounding circle of the optic nerve and the determination of vessel and nonvessel regions along the

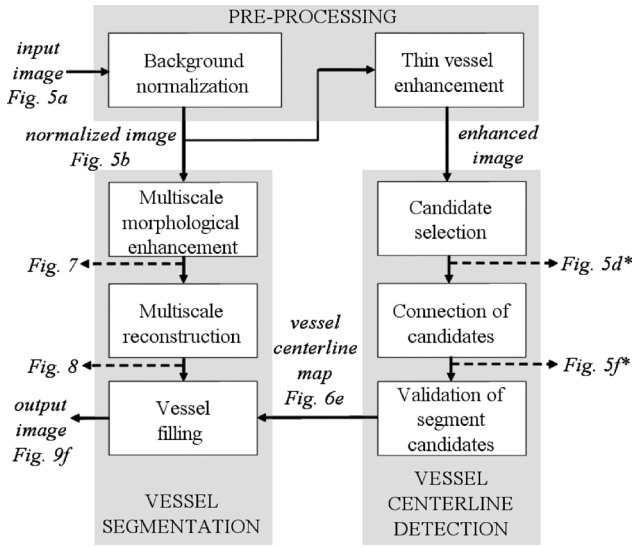


Fig. 1. Retinal vessel segmentation functional diagram (Notes: some of the block outputs point figures in subsequent sections; (\*) denotes images illustrating operations with horizontal vessels).

vessel profile is done using a fuzzy  $C$ -means clustering algorithm. The tracing method described in [39] automatically detects seed-tracking points, defined as local gray-level minima along a grid of one-pixel wide lines; then, a sequence of exploratory searches using a set of 2-D correlation kernels is executed aiming at detecting vessel boundaries; these templates are also recursively used for estimating the position and orientation of the next vessel point.

The method proposed in this paper follows a pixel processing-based approach. The initial step of vessel centerline detection combines local information, used for early pixel selection, with structural features, as the vessel length. Global intensity characteristics and local vessel width information are adaptively exploited in the subsequent vessel filling phase. Despite of the use of a few parameters, almost all algorithm settings are based on threshold values that are adaptively computed using local or global image dependent features.

### III. OVERVIEW OF THE VESSEL SEGMENTATION METHOD

The method herein presented can be schematically described by the functional block diagram in Fig. 1, where we identify three main processing phases: 1) preprocessing, for background normalization and thin vessel enhancement; 2) vessel centerline detection, for defining a set of connected segments in the central part of the vessels; and 3) vessel segmentation, for finally labeling the pixels belonging to the vessels. These phases are further subdivided in several steps, as follows:

**Preprocessing phase:** 1) *Background normalization*, which normalizes the monochromatic input image by subtracting an estimate of the background obtained by filtering with a large arithmetic mean kernel. 2) *Thin vessel enhancement* by processing with a set of line detection filters, corresponding to the four orientations  $0^\circ$ ,  $45^\circ$ ,  $90^\circ$ , and  $135^\circ$ ; for each pixel, the highest filter response is kept and added to the normalized image.

**Vessel centerline detection phase:** 1) *Selection of vessel centerline candidates*, using directional information provided from a set of four directional Difference of Offset Gaussians filters. 2) *Connection of the candidate points* obtained in the previous step, by a region growing process guided by some image statistics. 3) *Validation of centerline segment candidates* based on the characteristics of the line segments; this operation is applied in each one of the four directions and finally combined, resulting in the map of the detected vessel centerlines.

**Vessel segmentation phase:** 1) *Multiscale morphological vessel enhancement* by applying a modified top-hat transform with variable size structuring elements aiming at enhancing vessels with different widths. 2) *Multiscale morphological vessel reconstruction* by using a binary morphological reconstruction method, in order to obtain binary maps of the vessels at four scales. 3) *Vessel filling* by a region growing process using as initial seeds the pixels within the centerlines obtained in the vessel centerline detection phase; the growing is successively applied to the four scales and, in each growing region step, the seed image is the result of the previous aggregation.

Each one of these phases is detailed and illustrated in the next sections.

### IV. DETECTION OF VESSEL CENTERLINES

The green channel is considered in several works [5], [23], [31], [34] as the natural basis for vessel segmentation because it normally presents a higher contrast between vessels and retinal background. In this paper, we make use of other monochromatic components obtained from different color space representations, as it is discussed and justified in Section VI. Independently from the component derived from the original color fundus images, in our work the segmentation is always performed on a monochromatic image where the vessels show intensities higher than the background in order to make the representation of the vascular structures compatible with their appearance in retinal images obtained from an angiography.

Vessel centerlines are herein defined as connected sets of pixels which correspond to intensity maxima computed from the intensity profiles of the vessel cross sections. We may notice that, although this word may only convey a geometrical property (the line located at the center of the vessel), it is in fact derived from local intensity properties of the vessel cross profile taking advantage of the fact that the maximum local intensity usually occurs at the vessel central pixels. To locate candidate pixels belonging to the central part of a vessel, the original methodology developed by the authors for the detection of perifoveolar capillaries [40] was further adapted and extended. The underlying idea of this approach is that the response of directional differential operators, using kernels adapted to the local vessel direction, has opposite signs on the two hillsides of an ideal vessel cross profile; we will, therefore, explore this fact by considering the occurrence of specific combinations of filter response signs. To carry out the initial selection of the most likely centerline segments, the magnitude of the filter response is kept on the positions that verify one of the established sign conditions; this newly generated image is then segmented using region growing in order to retain just those points where restrictive intensity and connectivity conditions meet. For each one of these segments,

$$\frac{1}{6} \begin{bmatrix} -1 & -1 & -1 \\ 2 & 2 & 2 \\ -1 & -1 & -1 \end{bmatrix}; \frac{1}{6} \begin{bmatrix} -1 & -1 & 2 \\ -1 & 2 & -1 \\ 2 & -1 & -1 \end{bmatrix}; \frac{1}{6} \begin{bmatrix} -1 & 2 & -1 \\ -1 & 2 & -1 \\ -1 & 2 & -1 \end{bmatrix}; \frac{1}{6} \begin{bmatrix} 2 & -1 & -1 \\ -1 & 2 & -1 \\ -1 & -1 & 2 \end{bmatrix}$$

Fig. 2. Set of one-pixel width line detector filters used for thin vessel enhancement.

we compute the mean intensity, the maximum intensity, and the length of the pixel set; these features are further combined for final validation of the segments belonging to vessel centerlines. The detailed processing operations involved are described in the following subsections.

#### A. Image Preprocessing

The background of retinal images is often characterized by a gradual intensity variation occurring from the periphery of the retina towards the central macular area; other retinal regions, like the optic disc, also have distinctive intensity values. Vessels are retinal structures that stand out from the background, but a more thorough analysis of local vessel intensities can reveal significant variations (normally dependent from neighboring conditions) that can negatively interfere in the complete vessel segmentation process. In order to decrease this influence, the monochromatic representation of the original color image is normalized by subtracting an estimate of the background, which is the result of a filtering operation with a large arithmetic mean kernel.

As small vessels are very thin structures and usually present low local contrast, their segmentation is a difficult task. To improve the discrimination between these thin vessels and the background noise, the normalized image is processed with a set of line detection filters [41], corresponding to the four orientations  $0^\circ$ ,  $45^\circ$ ,  $90^\circ$ , and  $135^\circ$ . The set of convolution kernels used in this operation is shown in Fig. 2. For each pixel, the highest filter response is kept and added to the normalized image. This resulting image is the base of all subsequent operations used for the detection of vessel centerlines.

#### B. Detection of Centerline Segment Candidates

*1) Initial Selection of Candidate Points:* As previously mentioned, the first operation aiming at extracting vessel centerline pixels is the application of a set of directional differential filters sensitive to the main vessel orientations. The underlying idea is that when a first-order derivative filter is applied orthogonally to the main orientation of the vessel, derivative values with opposite signs are obtained on the two vessel hillsides, which simply means that there will be positive values on one side of the vessel cross section and negative values on the other. This idea is depicted in Fig. 3(a) for an ideal vessel cross profile, showing the expected signs of a derivative filter.

Since retinal vessels can occur in any direction, the selection of a set of directional filters whose responses can be combined to cover the whole range of possible orientations is required. We tested two ( $0^\circ$  and  $90^\circ$ ), four ( $0^\circ$ ,  $45^\circ$ ,  $90^\circ$ , and  $135^\circ$ ), and six ( $0^\circ$ ,  $30^\circ$ ,  $60^\circ$ ,  $90^\circ$ ,  $120^\circ$  and  $150^\circ$ ) directions and concluded that the solution based on four directions is an interesting trade-off between detection accuracy and computation time. The particular kernels used in this work are first-order derivative filters,



(a)

$$\begin{bmatrix} -1 & -2 & 0 & 2 & 1 \\ -2 & -4 & 0 & 4 & 2 \\ -1 & -2 & 0 & 2 & 1 \end{bmatrix}$$

(b)

(1)	++--
(2)	++-× and ADV > 0
(3)	×+- - and ADV < 0
(4)	+0--

(c)

Fig. 3. (a) Ideal vessel profile with expected derivative signs on opposite hillsides. (b) kernel of the DoOG filter used in this work with prevailing responses to vertical vessels. (c) Combinations of derivative signs and average derivative values that characterize the occurrence of a candidate centerline point: + means a positive derivative value; — means a negative value; 0 means a zero value; × is a do not care condition; ADV is the mean value of the derivative magnitudes calculated for the same set of four points where the specific combination of signs occurred.

known as difference of offset Gaussians filters (DoOG filters), with prevailing responses to horizontal ( $0^\circ$ ), vertical ( $90^\circ$ ), and diagonal ( $45^\circ$ ,  $135^\circ$ ) directions. These filters are used for the computation of the local image gradient in a specific direction, and have proved to be a good alternative to the more conventional solutions, as for instance, the Sobel kernels; in fact, the DoOG filters have demonstrated greater immunity to noise because they depend on larger kernel derivative filters. Each filter is the difference between two displaced copies of a Gaussian whose scale determines the DoOG kernel size [42]. The particular kernel used for detecting vertical centerline candidates is the row gradient filter presented in Fig. 3(b); the other three kernels are just rotated versions of this filter.

Each one of the four directional images resulting from the DoOG filters is searched for specific combinations of signs on the expected direction of the vessel cross section; the search is performed on one-pixel-wide lines with orientation corresponding to the vessel cross profile, which means that the scanning direction is distinct for each one of the four images under analysis. As real vessels do not have the ideal profile presented in Fig. 3(a), we empirically assessed several combinations of filter responses that can characterize a vessel and the result was the set of four combinations indicated in Fig. 3(c). In this figure, plus and minus signs correspond to positive and negative derivative responses, respectively, 0 is associated with a null output, and × is a do not care condition meaning that the sign of the derivative is not evaluated (conditions 2 and 3); however, in these two cases, the average value of the derivative magnitudes (ADV) for the intensity profile under analysis must be positive for condition 2, and negative for condition 3. The ADV value gives a good indication if the vessel is located in a region with slowly varying baseline on the vessel cross profile direction which can make the values of the derivatives dominantly positive (condition 2) or negative (condition 3).

To illustrate this process, consider the simple example for vessels with a vertical predominant orientation [those with the highest response to the row gradient filter of Fig. 3(b)]. We need to analyze the derivative signs on the direction of the vessel cross section (in this case, the horizontal direction, i.e., along

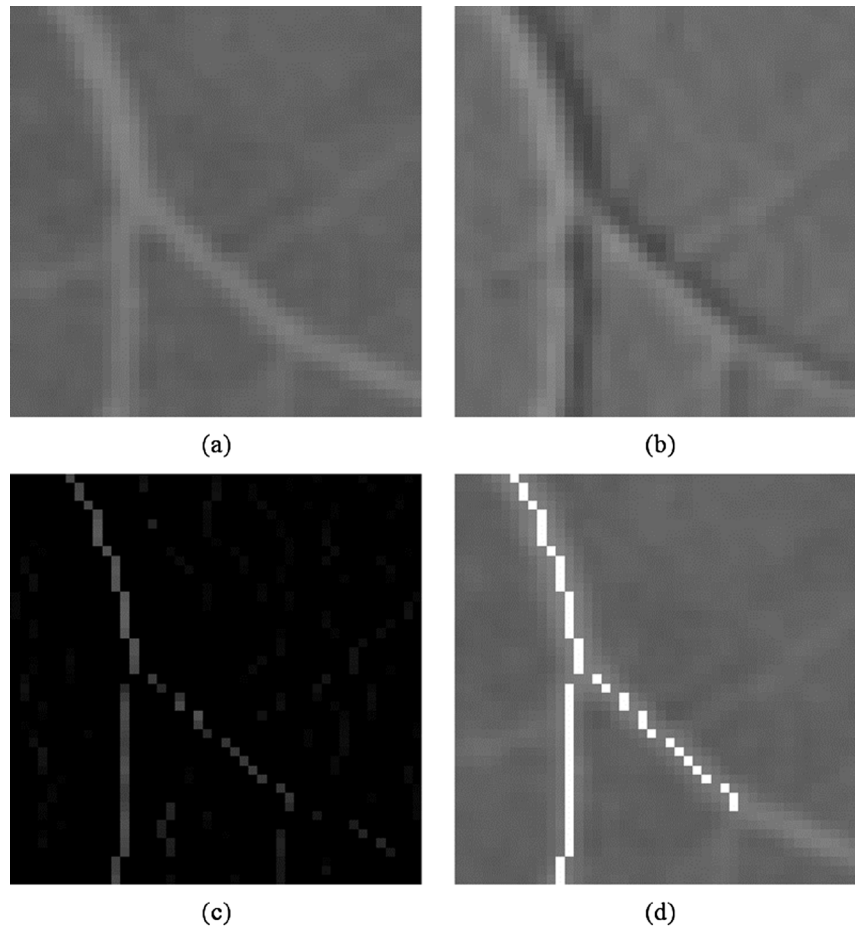


Fig. 4. Selection of candidate centerline points. (a) Fragment of the background normalized image that contains a vessel with dominant vertical direction. (b) Result of the DoOG row gradient filter (negatives values correspond to the lowest intensities and positive values correspond to the highest intensities). (c) Image with centerline candidates. (d) The image with centerline candidates was thresholded and overlapped on the normalized image.

the image rows) and to look for the particular combinations of derivative signs and ADV values indicated in Fig. 3(c). An occurrence of one of these combinations defines the loci of the centerline candidate in that particular segment of the image row, which will be constituted by four pixels for the first three conditions in Fig. 3(c) and by 3 three pixels in condition (4). The final centerline candidate is simply the pixel with the maximum intensity in the normalized image. This fact is registered in a new image by assigning at these coordinates the sum of the highest positive response with the absolute value of the most negative response; this particular arrangement of the two highest absolute filter responses was chosen because it provides a better discrimination between true and noisy points, since the sum acts as a kind of smoothing operator. The individual analysis of each image row assures that we will retain at most one candidate point for a particular vertical vessel cross profile; the result consists in several sets of connected segments, as other candidate points are naturally found on contiguous image rows. When the analysis of all image rows is concluded, this newly generated image will contain the candidate centerline points in the vertical direction, each one being characterized by a value proportional to the filter responses.

This procedure is illustrated in Fig. 4 for an image region containing a middle width vertical vessel. The top of the figure

shows the background normalized image [Fig. 4(a)] and the result of the filtering process using the row gradient filter [Fig. 4(b)]. The centerline candidates that are retained after the analysis of image rows are represented in Fig. 4(c); as previously mentioned, the intensity of each pixel is representative of the filter response. Finally, the adequacy of our methodology to locate points in the central part of the vessels can be confirmed in Fig. 4(d), that shows a thresholded version of Fig. 4(c) overlapped on the normalized image of Fig. 4(a); this last image clearly illustrates that those candidates associated with the highest filter responses are, as expected, effectively aligned with the central part of the vessel. The images presented in Fig. 4 also show that the row gradient kernel also responds to vessels with other directions than the vertical, which illustrates the overall coverage range of the four filters.

Similar procedures are used on the other three directions; the main differences are the kernels used for processing the images, and the distinctive directions that are searched for the occurrence of derivative sign combinations.

2) *Connection of Candidate Points:* Each one of the four images resulting from the sequence of operations described before is processed independently in order to produce a set of four-connected vessel segments with a common main orientation. This separate treatment of the four direction dependent filtering



results is crucial to our algorithm; if the directional results were combined before the validation phase, it would be very difficult to eliminate most of the noisy segments, at least using the simple features, such as length, that we have selected in this work. The problem is that many small noisy vessel-like structures, which are simple to eliminate in each individual image, are detected in more than one image and normally cross each other forming larger combinations of pixels; as a consequence, the combination of directional results would generate a mixture of the noisy segments, making the elimination process a much more difficult task. The union of the validated directional segments is executed only at the final stage of the complete centerline detection process.

From each image containing the selected set of candidate points in one specific direction, an initial collection of centerline segments is generated by a region growing process that is started with a set of seed points, verifying restricted value conditions, which are afterwards extended by aggregating other neighboring pixels with lower filter responses. Both seed and aggregation thresholds are defined based on statistics derived from the histogram of the image containing the set of candidate points; the values of the seeds are above a limit depending on the mean and standard deviation of this distribution, while aggregation threshold is the histogram mode. The threshold value,  $T_{\text{seed}}$ , for seed selection is evaluated by the function in (1). In this equation, the value of the coefficient  $\alpha$  is equal for all the images of the database, while  $\mu$  and  $\sigma$ , respectively, the mean and standard deviation of the distribution, are dependent on the properties of each particular image. It is worth stating that the value of  $\alpha$  to be settled for each image set depends mainly on the global intensity characteristics of the set

$$T_{\text{seed}} = \mu - \alpha\sigma. \quad (1)$$

A correct choice of this threshold value is critical for the elimination of noisy segments, usually found in the background and in other retinal structures, as the optic disc. However, if this value is too high, we may fail the detection of thin or low contrasted vessels. Similar considerations apply to the selection of the aggregation threshold, as a low value generally facilitates the aggregation of erroneous pixels, while a high value prevents the inclusion of valid vessel pixels.

The identification of the connected sets of points with a high probability of belonging to vessel centerlines is preceded by a cleaning of the smallest segments, while keeping those with more than a specified number of points ( $\text{min\_npoints}$ ); the value for this parameter is defined for the complete image set. To increase the discrimination between valid centerline segments and fragments associated with noise, each pixel of an image resulting from the region growing process is multiplied by the corresponding pixel value in the background normalized image. This operation is particularly important for pixels associated with thin vessels, where the values of directional gradients are similar to those in some background structures, but whose original intensities are usually higher.

The result of this processing sequence is a set of connected segments which needs further validation, as described in the

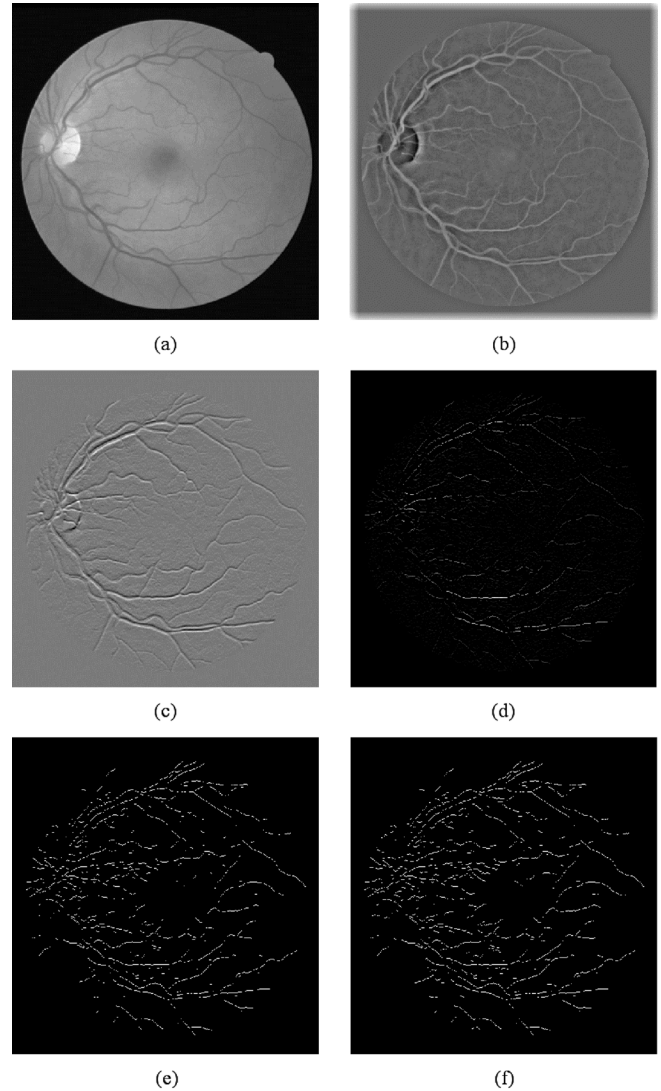


Fig. 5. (a) Graylevel intensity image obtained from an original color fundus image. (b) Background normalized image. (c) Result of the DoOG filter (horizontal vessels). (d) Initial set of candidate points (horizontal vessels). (e) Seed points (horizontal vessels). (f) Vessel centerline candidates (horizontal vessels).

next subsection. Fig. 5 illustrates some of the steps of this process in the horizontal direction, namely the response of the directional filter [Fig. 5(c)] and the initial set of candidate points that are retained after the search of filter response sign combinations [Fig. 5(d)]; Fig. 5(e) and (f), illustrating the region growing step, are presented in a binary form to increase the visibility.

### C. Validation of Centerline Segments

Every candidate segment is confirmed or rejected as a valid centerline segment based on two features:

- *Intensity of the segment*, evaluated by the geometric mean between the average and maximum intensity values of the segment; this is a tradeoff value between average and maximum, allowing a better foreground–background discrimination especially for low-contrasted vessels; when compared with other combinations, as the arithmetic mean, the geometric mean has proved to be less sensitive to noise.

- *Length of the segment*, measured by the number of points of the candidate segment; as pixel segments are linked using four-connectivity, the measured number of points is a good length estimate for the horizontal and vertical directions, but it is overestimated for diagonal segments; in this last case, the length value is approximated using a scaling factor equal to  $(\sqrt{2})^{-1}$ .

Each centerline candidate segment is validated by comparing its intensity and length features with image dependent reference values. As the validation process is applied independently to segments of the four directional sets, reference values for the two features, intensity and length, are calculated from each one of these sets. Global references for the two features are also obtained from a fifth set that gathers selected segments taken from the four directional sets; in this newly formed set, the segments keep all their individual characteristics except the direction. The herein used reference values are defined for each one of the five segment sets considered ( $h$ : horizontal;  $v$ : vertical;  $d_{45}$ : diagonal 45°;  $d_{135}$ : diagonal 135°;  $g$ : global).

The determination of the intensity reference for each one of the four directional sets follows a similar procedure. The first assumption is that all the segments with intensity features greater than an established threshold belong to a vessel, which means that all segments with intensity greater than this limit are immediately validated as centerline segments. As a consequence, the validation process is applied only to segments with intensities ranging from zero to that threshold; in this application, this limit was established as 30% of the maximum segment intensity of the corresponding set. The subsets constituted by those segments with restricted intensities are also the basis for the estimation of all reference values. The intensity reference associated with a particular directional set is defined as the difference between the mean and standard deviation of the distribution of the intensities of the corresponding subset; the global intensity reference is obtained following a similar process, but its value is derived from the union of the four subsets, as mentioned before. Each directional value for length comparison is just the mean of the subset length distribution, while the global reference is calculated based on their union.

The intensity and length reference values associated with direction  $x$ ,  $I_x^{\text{ref}}$  and  $L_x^{\text{ref}}$ , are defined, respectively, by (2) and (3). In these equations,  $I_x$  and  $L_x$  are, in that order, the directional intensity and length values calculated, as described before, from the subset of candidate segments with dominant direction  $x$ , while  $I_g$  and  $L_g$  are obtained from the union of the four subsets

$$I_x^{\text{ref}} = \max(I_x, I_g), \quad \text{for } x = h, v, d_{45}, d_{135} \quad (2)$$

$$L_x^{\text{ref}} = \max(L_x, L_g) \quad \text{for } x = h, v, d_{45}, d_{135}. \quad (3)$$

As it can be observed from these equations, the directional reference value is kept only if it is greater than the global one. This choice between directional and global reference values is fundamental to improve the removal of noisy segments, since a specific low directional reference, caused by an abnormal inclusion of non-vessel structures in a specific direction, is replaced by the global value, normally less sensitive to that kind of disturbances.

The classification of each individual segment  $s$  of a particular directional set  $x$  as a vessel centerline segment is based on the inequality presented in (4). In this equation, where a product rule is used for combining the two feature values,  $I_x^s$  and  $L_x^s$  are, respectively, the intensity and length features calculated for the segment  $s$ , and  $I_x^{\text{ref}}$ ,  $L_x^{\text{ref}}$  are the references obtained from (2) and (3) for the directional set  $x$  containing the segment under analysis

$$I_x^s \sqrt{L_x^s} \geq I_x^{\text{ref}} \sqrt{L_x^{\text{ref}}} \quad \text{for } x = h, v, d_{45}, d_{135}. \quad (4)$$

The option for a product rule, instead of a decision based on the comparison of the two features separately, has proved to be an important attribute as it allows an adaptive behavior of the classifier. Indeed, the product of the two reference values only establishes a limit that has to be fulfilled by the two segment features as a whole; therefore, it allows large segments to have smaller intensities, while it is especially restrictive when the length is less than an associated reference threshold. Equation (4) can be thought of as defining a variable threshold for intensities, where the highest values are associated with small length segments, while the lowest thresholds correspond to segments that contain a large number of points. In the same equation, we have adopted the square root of the length to represent this feature to avoid penalizing small segments, since large values for intensity would be required for a final classification as valid vessel segments. Similar considerations can be made regarding the decrease of the intensity level demanded for larger vessels, but this has no real influence because the high length segments normally present high intensity values too.

Following the independent evaluation of the four directional sets of segments, those segments classified as belonging to vessel centerlines are joined together into a binary image, being the final result of the process for vessel centerline detection. These results are depicted in Fig. 6, for the original fundus image of Fig. 5. The image represented in Fig. 6(a) shows the result of the horizontal centerline segment validation step as applied to the image of Fig. 5(f).

## V. VESSEL SEGMENTATION

With the aim of getting a complete segmentation of the retinal vessels, these structures need to be filled starting from the detected centerlines. For this purpose, a multiscale approach is followed, where a set of morphological operators with increasing structuring element size is used for generating several enhanced representations of the vascular network; each one of these images emphasizes vessels in a particular width range, from smaller to larger vessels. Image masks containing binary reconstructions of the main vessel segments within a specific size range are derived from the enhanced representations by morphological reconstruction. Vessel filling is achieved by an iterative procedure that, in each step, uses the output image from the previous iteration as seed for a simple region-growing algorithm, whose aggregation phase is limited by one of the above-mentioned binary masks.

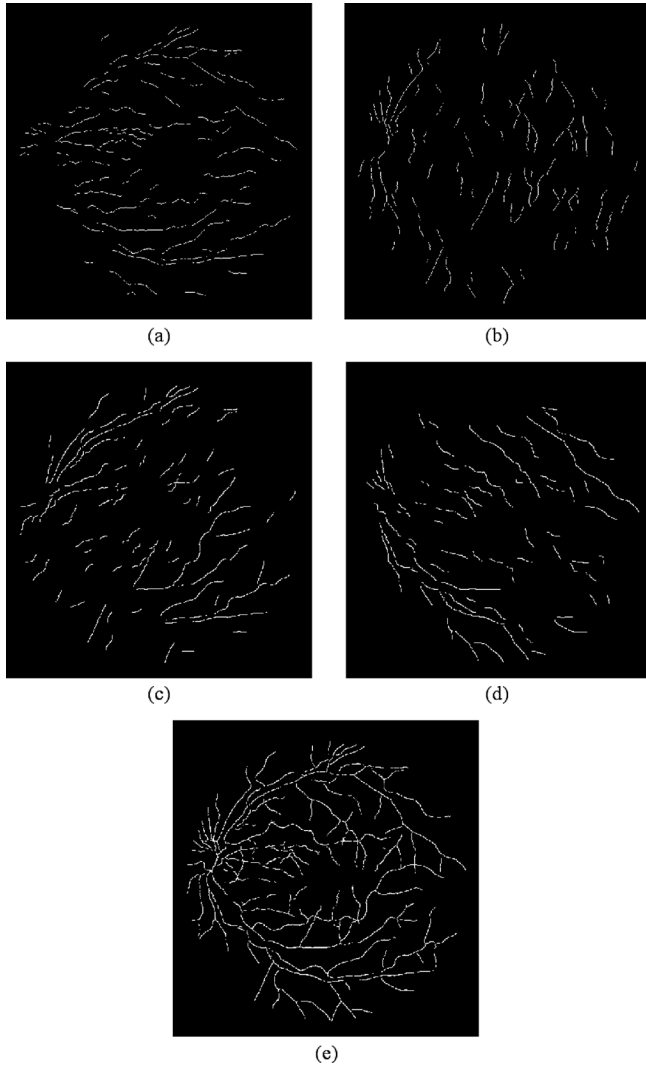


Fig. 6. (a)–(d) Vessel centerline segments (horizontal, vertical, diagonal 45°, diagonal 135°). (e) Detected vessel centerlines.

#### A. Vessel Enhancement

The use of morphological operators for segmenting vessels has already been reported [32] and [33]. In our method, the background normalized image is processed by a sequence of top-hat operators using circular structuring elements of increasing radius. The option for such a multiscale approach, instead of using a single monoscale operator, is justified by the expected dependence of the operator response from the vessel width. The range of the radius of the structuring elements varies from 1 to 8 pixels, covering the overall range of vessel widths for the two image datasets used in this work. For images with different scales, the set of structuring element radii should be adapted accordingly.

The classical top-hat transform is defined as the difference between an image and its opened version. A problem associated with this classical implementation is the sensitivity to noise, as a consequence of the fact that pixel values in an opened image are always less than or equal to the original ones; in such conditions, the difference image retains all small intensity fluctuations that can be found in the data. To overcome this inconvenience,

a modification was adapted from [43], by considering two new steps in the top-hat definition: a closing precedes the opening result which is followed by a comparison, using a minimum operator, to get an image equal to the original one everywhere except for peaks and ridges. Equation (5) represents this modified top-hat transform, where  $\mathbf{I}$  is the image to be processed, while  $S_c$  and  $S_o$  stand for the structuring elements for closing ( $\bullet$ ) and opening ( $\circ$ ) operators, respectively

$$\text{TopHat}_{\mathbf{I}} = \mathbf{I} - \min((\mathbf{I} \bullet S_c) \circ S_o; \mathbf{I}). \quad (5)$$

The closing operation is intended to generate a smoothed version of the original data, where the details smaller than the structuring element are replaced by higher nearby intensities. The opened image essentially maintains the pixel values, while eliminating more intense image regions with sizes smaller than the structuring element size. The final result of the comparison and subtraction is an enhanced image that mostly retains the original image regions with size smaller than the structuring element which show significant local intensity variations.

To obtain a multiscale representation of the retinal vascular structure, we apply the modified top-hat transform to the background normalized image, using circular structuring elements of increasing radius, ranging from 1 to 8 pixels. In the operator proposed in [43], identical structuring elements were used for the closing and opening operations. Nevertheless, in our implementation, we have decided to use different kernel sizes because the goals of the two morphological operations are different; while closing is intended to eliminate background fluctuations, thus suggesting small size structuring elements, opening aims at removing vessels, which motivated the use of several structuring elements with different sizes. Consequently, as the radius of circular structuring element for the opening is progressively increased, the radius of the circular kernel for the closing is kept constant and equal to the smallest size of 1 pixel.

The eight images at various scales are finally reduced to four, each one obtained as the average of the two responses of operators with consecutive radii. The observation that most vessels have significant responses to more than one morphological filter could have led to a small set of operators, using for instance an increased step for the generation of successive structuring elements. Instead, we have decided to keep the eight kernels and combine their responses since the averaging operation improves the signal-to-noise ratio of the resulting image, thus facilitating the discrimination between vessels and other background structures.

As a consequence of the distinct size of the structuring elements, each image is adapted to highlight vessels within a limited range of widths. Essentially, the images obtained with the smallest structuring elements just retain correct width data for small vessels, since only the central part of the other vessel segments is represented. On the other hand, larger structuring elements are able to extract larger vessels, but thinner structures are naturally blurred. These facts can be observed in Fig. 7, showing two images that are combinations of results of the top-hat operators, obtained using the smallest and largest structuring elements for the opening operator. Fig. 7(a) presents the average of the enhanced images obtained with the circular structuring



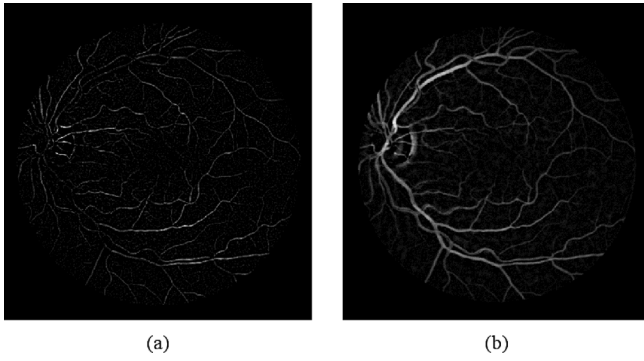


Fig. 7. Outputs of the modified top-hat operator for the image of Fig. 5. (a) Result using circular structuring elements with radius 1 and 2. (b) Result using circular structuring elements with radius 7 and 8.

elements of 1 and 2 pixel radii, while the combination of the results using the 7 and 8 pixel radii structuring elements is shown in Fig. 7(b).

### B. Vessel Segment Reconstruction

The four images resulting from the previous processing sequence are used for reconstructing potential vessel segments. For this task, we selected a binary morphological reconstruction method, called the double threshold operator. This operator consists in thresholding each image for two ranges of gray values, one being included in the other. The image obtained with the narrow threshold range (*marker* image) is used as a seed for the reconstruction using the wide range thresholded image (*mask* image) [44].

This morphological operator is used to reconstruct vessel segments from each one of the four enhanced vessel representation. Based on the distinct emphasis put on different widths by each specific top-hat transform, a correct selection of the *marker* and *mask* images allows the generation of four binary images, each one containing a partial reconstruction of the vascular tree of the retina. For each vessel enhanced image, we obtain the *marker* and *mask* images using threshold values derived from the intensity histogram of the non-null pixels; each one of these thresholds is defined as the highest intensity value such that the number of pixels with intensities above this limit is greater or equal to a predefined percentage. Fig. 8 shows the *marker* and *mask* images derived from the two top-hat images of Fig. 7, as well as the outputs of the morphological reconstruction operator. These results illustrate the superior performance of the reconstruction when compared to a simple thresholding operation, represented in this figure by the *mask* image. These results also show the vessel width selectivity of the proposed methodology.

### C. Vessel Filling

We obtain a final image with the segmented vessels by iteratively combining the centerline image with the set of images that resulted from the vessel segments reconstruction phase.

In the first iteration, vessel centerline pixels are used as seeds for a region growing algorithm, which breed these points by aggregating the pixels in the reconstructed image derived from the top-hat operator with the smallest structuring element size.

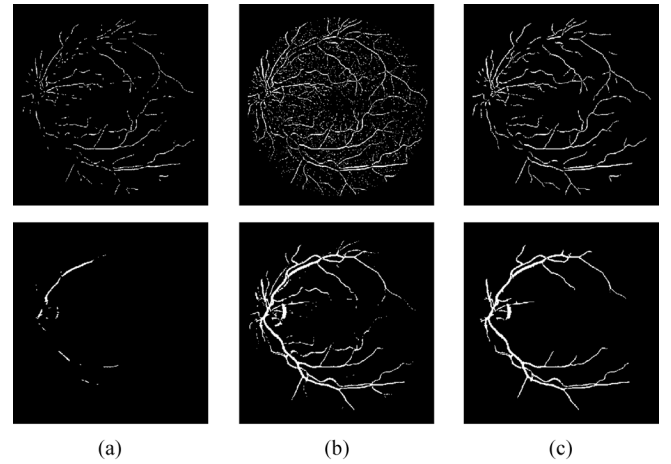


Fig. 8. Results of the morphological reconstruction operator for the enhanced images of Fig. 7(a) (top row) and Fig. 7(b) (bottom row). (a) *Marker* image. (b) *Mask* image. (c) Output of the morphological reconstruction operator.

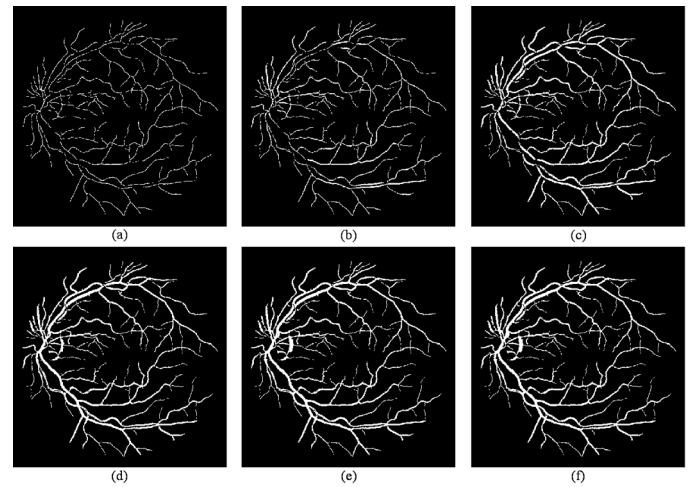


Fig. 9. Intermediate and final results of the vessel filling phase for the original image of Fig. 5(a). (a) *Vessel centerlines*. (b)-(e) Intermediate results. (f) Final result of the vessel segmentation process.

The aggregation of points is, as usual, conditioned by the connectivity restriction. In each of the subsequent three iterations, the reconstructed images corresponding to the vessels with increasing width are in turn used for extending the output of the previous region growing step.

The final vessel segmentation is obtained after a cleaning operation aiming at removing all pixels completely surrounded by vessel points, but not labeled as part of a vessel. This is done by considering that each pixel with at least six neighbors classified as vessel points must also belong to a vessel. The intermediate and final results of the iterative vessel filling phase are illustrated in Fig. 9.

## VI. RESULTS

The method described in the previous sections was tested on images of two publicly available databases, the DRIVE database and the STARE database.

The DRIVE database contains 40 color images of the retina, with  $565 \times 584$  pixels and 8 bits per color channel, represented

in LZW compressed TIFF format. These images were originally captured from a Canon CR5 nonmydriatic 3 charge-coupled device (CCD) camera at 45° field of view, and were initially saved in JPEG-format. Besides the color images, the database includes masks with the delimitation of a field of view (FOV) of approximately 540 pixels in diameter for each image, and binary images with the results of manual segmentation. These binary images have already been used as ground truth for performance evaluation of several vessel segmentation methods [34]. The 40 images were divided into a training set and a test set by the authors of the database. The results of the manual segmentation are available for all the images of the two sets. For the images of the test set, a second independent manual segmentation also exists. To evaluate the performance of our approach, all the 40 images of the database were tested; however, as only the results for the test set are accessible at the database site [45], we will also report the values for this restricted set.

The other 20 image set, originally collected by Hoover *et al.* [23], was obtained from the STARE database [46]. These retinal images were captured using a TopCon TRV-50 fundus camera at 35° FOV, and afterwards digitized to 700 × 605 pixels, 8 bits per RGB channel. Binary images with manual segmentations are available for each image of the set. We derived the mask images from the matched spatial filter (MSF) images accessible at the STARE project website, with an approximate 650 × 550 diameter FOV. While the complete DRIVE set contains only seven pathological cases (four on the test set and three on the training set), 10 abnormal images are included in the 20 image set collected by Hoover *et al.*

#### A. Selection of the Monochromatic Image Representation

As previously mentioned, the use of several monochromatic representations of the original color images was explored in order to evaluate their adequacy for the segmentation of the retinal vascular network. Though the selection of the green channel of the RGB representation is a natural choice for this kind of application, justified by the high contrast between vessels and their background, other alternatives are also possible depending on the characteristics of the original color images.

In this work, the assessed representations were the green component of the original RGB image, the luminance channel of the National Television Systems Committee (NTSC) color space, and the  $a^*$  component of the  $L^*a^*b^*$  representation; in this last color coordinate system, the  $a^*$  component is correlated with the red (R) and green (G) channels of the RGB representation [41]. Examples of these three representations are presented in Fig. 10 for two original color images, one taken from the DRIVE database (top) and the other from the STARE database (bottom). As it can be observed, the green component shows a higher contrast than the luminance channel, and this conclusion can be generalized for most of the images of both databases. Still, for the images of the STARE database, the vessels in the component derived from the  $L^*a^*b^*$  representation clearly stand out from the background, as shown in Fig. 10. The  $L^*a^*b^*$  channel images for the DRIVE database did not present enough quality for a vascular segmentation task; in our opinion, this fact can be associated with the JPEG format that was initially used for storing the images.

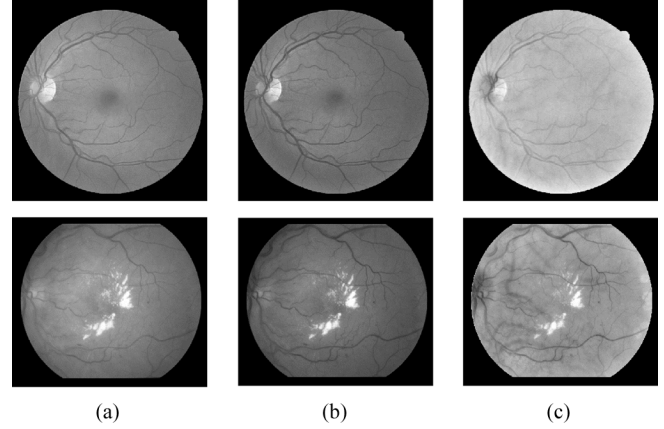


Fig. 10. Top row: normal image of the DRIVE database. Bottom row: pathological image of the STARE database. (a) Luminance image. (b) Green-channel image. (c)  $a^*$  component of the  $L^*a^*b^*$  representation.

TABLE I  
VALUES OF THE PARAMETERS USED FOR RETINAL VESSEL SEGMENTATION

Parameter		DRIVE images	STARE images
$\alpha$		0.1	- 0.1
$min\_npoints$		15	18
Histogram % (marker image)	$R_1=1; R_2=2$	10/25	10/15
	$R_3=3; R_4=4$	10/20	10/15
Histogram % (mask image)	$R_5=5; R_6=6$	5/15	5/10
	$R_7=7; R_8=8$	1/10	5/10

#### B. Settings

The experiments with our method were implemented using the settings included in Table I. Some of the values are different for the images of the two databases, as they were estimated from a set of five images taken from each database.

The kernel size of the average filter used in the background normalization was set as 31 for both databases. Vessel centerlines were extracted with the values shown in Table I for the parameter  $\alpha$ , used for selecting the initial seed set (1), and the minimum number of points required for a connected set to be accepted as a vessel segment candidate,  $min\_npoints$ . The selection of these two parameters was mainly a trade-off between the detection of thin vessels and noise immunity. All the other settings used in the centerline algorithm are adaptively computed from the particular image to be segmented.

The vessel filling phase parameters are the eight histogram percentages used in vessel reconstruction; this predetermined histogram percentages define image dependent threshold values needed for generating the *marker* and *mask* images. The associated structuring element radii ( $R_i = i, i = 1 \dots 8$ ) are also indicated in Table I.

#### C. Performance Measures

The method for the automatic segmentation of the retinal vasculature was evaluated on the images of the DRIVE and STARE databases. To facilitate the comparison with other retinal vessel segmentation algorithms, we have selected the segmentation accuracy as performance measure. The accuracy is estimated by

TABLE II  
PERFORMANCE OF VESSEL SEGMENTATION METHODS (DRIVE IMAGES)

Method	Average Accuracy (standard deviation)	True positive fraction	False positive fraction
2 <sup>nd</sup> Human observer [45]	0.9473 (0.0048)	0.7761	0.0275
Mendonça (gray-intensity)	0.9463 (0.0065)	0.7315	0.0219
Mendonça (green-channel)	0.9452 (0.0062)	0.7344	0.0236
Staal [5], [45]	0.9442 (0.0065)	0.7194	0.0227
Niemeijer [34], [45]	0.9417 (0.0065)	0.6898	0.0304

TABLE III  
PERFORMANCE OF VESSEL SEGMENTATION METHODS (STARE IMAGES;  
WITH FOV)

Method	Average Accuracy (standard deviation)	True positive fraction	False positive fraction
2 <sup>nd</sup> Human observer	0.9354 (0.0171)	0.8949	0.0610
Mendonça ( $a^*$ component)	0.9479 (0.0123)	0.7123	0.0242
Mendonça (luminance)	0.9421 (0.0151)	0.6764	0.0266
Mendonça (green)	0.9440 (0.0142)	0.6996	0.0270
Hoover [23], [46]	0.9267 (0.0099)	0.6751	0.0433
Staal [5]	0.9516 (not available)	0.697	0.019

the ratio of the total number of correctly classified points (sum of true positives and true negatives) by the number of points in the image FOV. Other important measures are sensitivity and specificity, which are indicators of the number of properly classified pixels, respectively in the true positive and true negative classes. Sensitivity is also known as true positive fraction, while the true negative fraction, which stands for the fraction of pixels erroneously classified as vessel points, is associated with specificity. The gold standard for computing the performance measures was a manual segmentation result provided together with each database image.

Table II presents the maximum average accuracy and standard deviation calculated with our method for the test set of the DRIVE database, using both the gray intensity and the green-channel images; the values for the fraction of pixels erroneously classified as vessel pixels [false positive fraction (FPF)] and for the percentage of pixels correctly classified as vessel pixels (true positive fraction) are also shown. The two set of results were calculated using the parameters presented in Table I. The same performance measures for other vessel segmentation methods, as obtained from the DRIVE database site [45], are also shown in Table II. All reported results were calculated for the 20 images of the test set.

The results obtained for the 20-image set of the STARE database are shown in Table III. As in the DRIVE database, the same set of parameters was used for calculating the mean values of the performance measures for the three monochromatic representations. The values reported for the Hoover *et al.* method [23] were determined using the segmented images downloaded from the STARE project website [46] based on the same FOV masks that we have used to generate our results. The average accuracy

TABLE IV  
PERFORMANCE OF VESSEL SEGMENTATION METHODS (STARE  
IMAGES—NORMAL VERSUS ABNORMAL CASES)

Method	Average Accuracy (standard deviation)	True positive fraction	False positive fraction
Normal cases			
2 <sup>nd</sup> Human observer	0.9283 (0.0100)	0.9646	0.0764
Mendonça ( $a^*$ component)	0.9531 (0.0119)	0.7366	0.0178
Mendonça (luminance)	0.9477 (0.0129)	0.7109	0.0206
Mendonça (green)	0.9492 (0.0122)	0.7258	0.0209
Hoover [23], [46]	0.9324 (0.0072)	0.6766	0.0338
Abnormal cases			
2 <sup>nd</sup> Human observer	0.9425 (0.0208)	0.8252	0.0456
Mendonça ( $a^*$ component)	0.9426 (0.0107)	0.6801	0.0306
Mendonça (luminance)	0.9364 (0.0156)	0.6420	0.0326
Mendonça (green)	0.9388 (0.0150)	0.6733	0.0331
Hoover [23], [46]	0.9211 (0.0091)	0.6736	0.0528

TABLE V  
PERFORMANCE OF VESSEL SEGMENTATION METHODS (STARE IMAGES;  
FPF = 4.4%; NO FOV)

Method	True positive fraction
2 <sup>nd</sup> Human observer	0.895
Mendonça ( $a^*$ component)	0.842
Mendonça (luminance)	0.807
Mendonça (green)	0.828
Hoover [23]	0.75
Jiang [31]	0.835

reported by Staal in [5] is higher but, as mentioned by the authors, they used only 19 of the 20 images in the STARE database; of these ten were normal and nine were pathological. In order to demonstrate the performance of our method in pathological cases, the values obtained for the green-channel of the STARE images for the normal and abnormal sets are discriminated in Table IV.

To facilitate the comparison of our results with those presented by Hoover *et al.* [23] and Jiang *et al.* [31] in their original papers, we have replicated the computation conditions by including the calculation of the average true positive fraction for the false positive fraction of the second hand-labeled image set, and by considering all image pixels (without any FOV). Each true positive fraction result included in Table V corresponds to a false positive fraction of 0.044, which was the value reported by Jiang *et al.* [31] and confirmed by us using the second set of hand segmented images available on the STARE project website. The performance measures of our method are the average values for the whole set of 20 images, derived from receiver operating characteristic (ROC) analysis based on a linear setting of the eight-parameter set used in the control the vessel filling phase.

Vessel segmentation results for the DRIVE and STARE sets are illustrated in Figs. 11 and 12, respectively. Both figures illustrate the vessel centerlines, final vessel segmentation, and

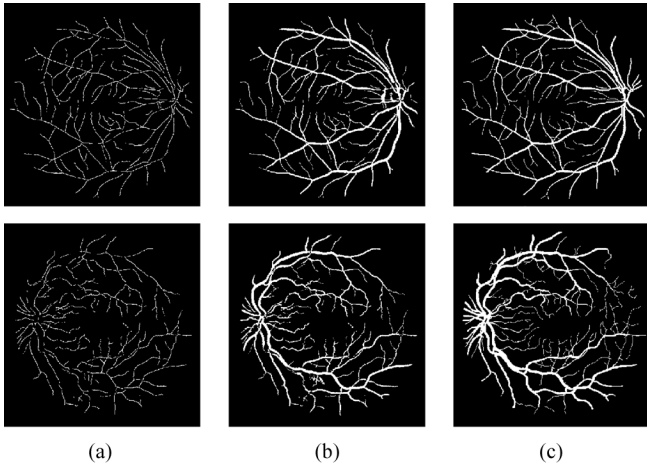


Fig. 11. Top row: best result for the DRIVE set (accuracy = 0.9633). Bottom row: worst result for the DRIVE set (accuracy = 0.9336). (a) Vessel centerlines. (b) Final vessel segmentation. (c) Ground truth image.

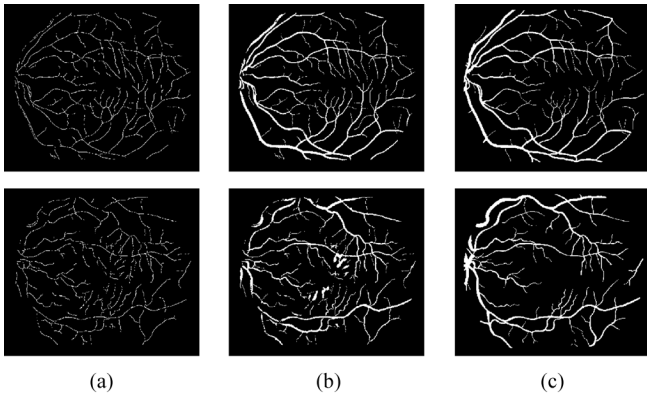


Fig. 12. Top row: normal case of the STARE set (accuracy = 0.9579). Bottom row: pathological case of the STARE set (accuracy = 0.9353). (a) Vessel centerlines. (b) Final vessel segmentation. (c) Ground truth image.

ground truth images. Fig. 11 shows the best and worst accuracy results using the proposed method for the DRIVE images. The top part of Fig. 12 presents a normal case, while the segmentation results for the pathological case depicted in Fig. 10 can be observed in the bottom. Finally, Fig. 13 illustrates the segmentation results for the three monochromatic representations for the STARE image set, using once again the pathological image of Fig. 10.

## VII. DISCUSSION AND CONCLUSION

The method proposed in this paper has proved to be a valuable tool for the segmentation of the vascular network in retinal images. The results reported in Tables II–IV show that, if the maximum average accuracy is used as performance measure, the values achieved with our algorithm are comparable, and in some cases, even exceed recently published results, and approximate to the performance of human observers. It is important to notice that the average values for sensitivity and specificity, which assess the agreement of the individual pixel classification with the ground truth vessel and nonvessel classes, respectively, are, in most cases, higher than those reported by other authors.

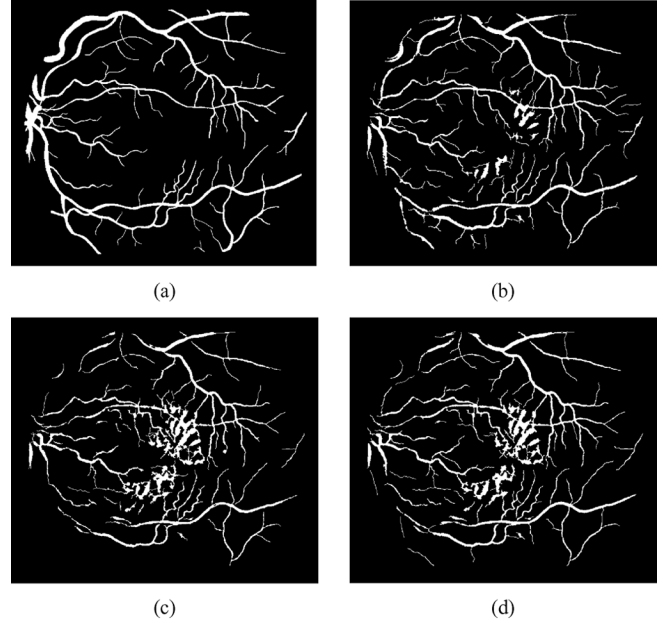


Fig. 13. Abnormal case of the STARE set. (a) Ground truth image. (b) Vessel segmentation using the  $a^*$  component of the  $L^*a^*b^*$  representation. (c) Vessel segmentation using the gray-intensity image (worst result for the set). (d) Vessel segmentation using the green channel (worst result for the set).

Table II gives an overview of the segmentation results for the DRIVE images. The average accuracy values of our algorithm outperform the proposals of Staal [5] and Niemeijer [34] even for green channel images. Wilcoxon matched pairs tests [47] on the accuracy of individual images demonstrate that our results for the gray-intensity images are significantly different from the method of Niemeijer ( $p < 0.001$ ) and from the method of Staal ( $p < 0.02$ ), being comparable only with the second human observer ( $p = 0.18$ ). The values for green channel images show a significant difference ( $p < 0.005$ ) when compared with those of Niemeijer, but there was no significant difference with the method of Staal.

Tables III and IV show the performance results for the STARE images. Our method performs significantly better than the proposal of Hoover [23] ( $p < 0.001$ ), both for normal and pathological images. The average accuracy reported by Staal is higher [5] but, as mentioned by the authors, they used only 19 (ten normal and nine with pathology) of the 20 images in the STARE database. As expected, the average values of accuracy, true positive fraction and false positive fraction are different for normal and abnormal cases; however, as shown in Table IV, our performance measures for the pathological set are still higher than those achieved by the Hoover *et al.* method for the normal images. The results presented in Table V were obtained after replicating the computation conditions reported in [23] and [31]. Our method outperforms the Hoover *et al.* algorithm, but only the true positive fraction for the  $a^*$  component is higher than the value obtained by Jiang *et al.* Nevertheless, all the results in this table correspond to a false positive fraction which is not realistic for our method, as the false positive rates, calculated without FOV for the three types of images that we have tested, are less than 2%.

An interesting conclusion of this work is that for well contrasted images, as it happens with those in DRIVE database, the use of the luminance image can be a good alternative to the green channel because the performance of the centerline detection algorithm is, in general, less sensitive to the background noise, which is more intense in the green channel. For the STARE database images, the  $a^*$  component of the  $L^*a^*b^*$  representation demonstrated higher performance than both green and luminance channels.

Our method can be classified as a pixel processing-based approach. The initial step of vessel centerline detection combines local information, used for early pixel selection, with structural features, as the vessel length. Global intensity characteristics and local vessel width information are adaptively exploited in the subsequent vessel filling phase. A major feature of the method is its adaptability to particular image intensity properties, as most algorithm settings are based on threshold values computed from local or global image information.

When compared with other vessel segmentation approaches, the present proposal assigns a hard classification result to each image point. As an alternative, the association of a value representing the probability of belonging to a vessel can be an interesting characteristic of a segmentation methodology.

The detection of vessel centerlines is an essential step that conditions the overall segmentation results. As a matter of fact, the use of the retinal vasculature skeleton has several advantages, mainly the exclusion of noisy segments and the accurate detection of thin vessels. However, as a consequence of the aggregation process used in the filling phase, when a vessel centerline is missing, the corresponding segmented vessel normally is not included in the final segmentation result.

In the images illustrating the detection of vessel centerlines (Figs. 6, 11, and 12), we may observe some fragmentation in the centerlines of the largest vessels. This is a consequence of the rule adopted for associating the centerline point with the position of the highest intensity value in the vessel profile. This rule favors the accurate localization of thin vessels, but it is very penalizing for larger ones, that often present a decrease of intensity in the center of the vessel, known as central reflex [48]; when this situation occurs, the centerline candidate segments are sometimes fragmented, and the small segments are frequently removed in the initial steps of the process. Other solutions, as the localization of centerline candidates in the position of the highest positive (or negative) value of the derivative filter response, are able to improve the continuity of large vessels centerline segments, but the accuracy of thin vessel segmentation is clearly poorer.

If we assess qualitatively the segmentation results, the main types of error that we may find are: 1) detection of other retinal structures, like the optic disc, several pathological areas and background structures; 2) undersegmentation of some vessel segments; 3) partial, or complete, missing of thin vessel branches. The first and third types of error are normally related with the centerline detection phase, and most of the times are interconnected. Actually, the derivative operators used for centerline point localization also generate significant responses in regions with severe intensity transitions, as those in the optic disc boundaries or near lesion borders; in order to minimize the

inclusion of such erroneous segments, a restrictive selection strategy was chosen, with the expected consequences in thin low-contrasted vessels. Even though a part of the optic disc border is sometimes visible in some of the segmented images, as the vessel filling process tends to deteriorate this situation. The undersegmentation of vessel regions occurred in just a few images as a consequence of the variability of intensity and contrast among vessels or vessel regions. Although most of these variations are naturally compensated by the vessel enhancement step, the need to discriminate between valid segments and background noise prevents the reconstruction of some vessel areas. Some of the above-mentioned misdetections can be minimized, or even eliminated, if a more flexible classification process is considered for every image point, instead of the present vessel/nonvessel labeling. An initial localization of the optic disc can also attenuate the incorrect classification in this region, and could improve the global performance of the method.

The processing time of our algorithm is less than 2.5 min for an image of the DRIVE database, and less than 3 min for a STARE image, on a Pentium-4 PC, running at 3.2 GHz, with 960 Mb of RAM images. The method is currently implemented using MatLab.

#### ACKNOWLEDGMENT

The authors would like to thank the authors of DRIVE and STARE databases for making their data publicly available. The authors would also like to thank Dr. J. R. Nunes from the Department of Ophthalmology, Santo António Hospital, Porto, Portugal, for his clinical advice.

#### REFERENCES

- [1] D. E. Becker, A. Can, J. N. Turner, H. L. Tanenbaum, and B. Roysam, "Image processing algorithms for retinal montage, synthesis, mapping and real-time location determination," *IEEE Trans. Biomed. Eng.*, vol. 45, no. 1, pp. 115–118, Jan. 1998.
- [2] L. Zhou, M. S. Rzeszutarski, L. J. Singerman, and J. M. Chokreff, "The detection and quantification of retinopathy using digital angiograms," *IEEE Trans. Med. Imag.*, vol. 13, no. 4, pp. 619–626, Dec. 1994.
- [3] T. Teng, M. Lefley, and D. Claremont, "Progress towards automated diabetic ocular screening: A review of image analysis and intelligent systems for diabetic retinopathy," *Med. Biol. Eng. Comput.*, vol. 40, pp. 2–13, 2002.
- [4] R. M. Cesar, Jr and H. F. Jelinek, "Segmentation of retinal fundus vasculature in nonmydriatic camera images using wavelets," in *Angiography and Plaque Imaging. Advanced Segmentation Techniques*, J. S. Suri and S. Laxminarayan, Eds. Boca Raton, FL: CRC, 2003, pp. 193–224.
- [5] J. Staal, M. D. Abramoff, M. Niemeijer, M. A. Viergever, and B. van Ginneken, "Ridge-based vessel segmentation in color images of the retina," *IEEE Trans. Med. Imag.*, vol. 23, no. 4, pp. 501–509, Apr. 2004.
- [6] C. Heneghan, J. Flynn, M. O'Keefe, and M. Cahill, "Characterization of changes in blood vessel width and tortuosity in retinopathy of prematurity using image analysis," *Med. Image Anal.*, vol. 6, pp. 407–429, Dec. 2002.
- [7] A. J. Campilho, A. M. Mendonça, and J. R. Nunes, "Image analysis techniques for avascular region detection in retinal angiography," in *Proc. ICIAP*, 1992, pp. 624–628.
- [8] E. Grisan and A. Ruggeri, "A divide and impera strategy for the automatic classification of retinal vessels into arteries and veins," in *Proc. 25th Int. Conf. IEEE Eng. Med. Biol. Soc.*, 2003, pp. 890–893.
- [9] Y. Hatanaka, H. Fujita, M. Aoyama, H. Uchida, and T. Yamamoto, "Automated analysis of the distributions and geometries of blood vessels on retinal fundus images," *Proc. SPIE Med. Imag. 2004: Image Process.*, vol. 5370, pp. 1621–1628, 2004.

- [10] M. Foracchia, E. Grisan, and A. Ruggeri, "Extraction and quantitative description of vessel features in hypertensive retinopathy fundus images," in *Book Abstracts 2nd Int. Workshop Comput. Asst. Fundus Image Anal.*, 2001, p. 6.
- [11] X. Goa, A. Bharath, A. Stanton, A. Hughes, N. Chapman, and S. Thom, "A method of vessel tracking for vessel diameter measurement on retinal images," in *Proc. ICIP*, 2001, pp. 881–884.
- [12] M. E. Martinez-Perez, A. D. Hughes, A. V. Stanton, S. A. Thom, N. Chapman, A. A. Bharath, and K. H. Parker, "Retinal vascular tree morphology: A semiautomatic quantification," *IEEE Trans. Biomed. Eng.*, vol. 49, no. 8, pp. 912–917, Aug. 2002.
- [13] J. Lowell, A. Hunter, D. Steel, A. Basu, R. Ryder, and R. L. Kennedy, "Measurement of retinal vessel widths from fundus images based on 2-D modeling," *IEEE Trans. Med. Imag.*, vol. 23, no. 10, pp. 1196–1204, Oct. 2004.
- [14] H. Shen, B. Roysam, C. V. Stewart, J. N. Turner, and H. L. Tanenbaum, "Optimal scheduling of tracing computations for real-time vascular landmark extraction from retinal fundus images," *IEEE Trans. Inf. Technol. Biomed.*, vol. 5, no. 1, pp. 77–91, Mar. 2001.
- [15] A. Pinz, S. Bernogger, P. Datlinger, and A. Kruger, "Mapping the human retina," *IEEE Trans. Med. Imag.*, vol. 17, no. 4, pp. 606–619, Aug. 1998.
- [16] F. Zana and J. C. Klein, "A multimodal registration algorithm of eye fundus images using vessels detection and Hough transform," *IEEE Trans. Med. Imag.*, vol. 18, no. 5, pp. 419–428, May 1999.
- [17] A. Can, C. V. Stewart, B. Roysam, and H. L. Tanenbaum, "A feature-based, robust, hierarchical algorithm for registering pairs of images of the curved human retina," *IEEE Trans. Pattern Anal. Mach. Intell.*, vol. 24, no. 3, pp. 347–364, Mar. 2002.
- [18] C.-L. Tsai, C. V. Stewart, H. L. Tanenbaum, and B. Roysam, "Model-based method for improving the accuracy and repeatability of estimating vascular bifurcations and crossovers from retinal fundus images," *IEEE Trans. Inf. Technol. Biomed.*, vol. 8, no. 2, pp. 122–130, Jun. 2004.
- [19] K. H. Fritzsche, A. Can, H. Shen, C.-L. Tsai, J. N. Turner, H. L. Tanenbaum, C. V. Stewart, and B. Roysam, "Automated model-based segmentation, tracing and analysis of retinal vasculature from digital fundus images," in *Angiography and Plaque Imaging. Advanced Segmentation Techniques*, J. S. Suri and S. Laxminarayan, Eds. Boca Raton, FL: CRC, 2003, pp. 225–297.
- [20] A. Hoover and M. Goldbaum, "Locating the optic nerve in a retinal image using the fuzzy convergence of the blood vessels," *IEEE Trans. Med. Imag.*, vol. 22, no. 8, pp. 951–958, Aug. 2003.
- [21] M. Foracchia, E. Grisan, and A. Ruggeri, "Detection of the optic disc in retinal images by means of a geometrical model of vessel structure," *IEEE Trans. Med. Imag.*, vol. 23, no. 10, pp. 1189–1195, Oct. 2004.
- [22] H. Li and O. Chutatape, "Automated feature extraction in color retinal images by a model based approach," *IEEE Trans. Biomed. Eng.*, vol. 51, no. 2, pp. 246–254, Feb. 2004.
- [23] A. Hoover, V. Kouznetsova, and M. Goldbaum, "Locating blood vessels in retinal images by piecewise threshold probing of a matched filter response," *IEEE Trans. Med. Imag.*, vol. 19, no. 3, pp. 203–211, Mar. 2000.
- [24] Y. Sun, "Automated identification of vessel contours in coronary arteriograms by an adaptive tracking algorithm," *IEEE Trans. Med. Imag.*, vol. 8, no. 1, pp. 78–88, Mar. 1989.
- [25] K. A. Vermeer, F. M. Vos, H. G. Lemij, and A. M. Vossepoel, "A model based method for retinal blood vessel detection," *Comput. Biol. Med.*, vol. 34, pp. 209–219, 2004.
- [26] S. Chaudhuri, S. Chatterjee, N. Katz, M. Nelson, and M. Goldbaum, "Detection of blood vessels in retinal images using two-dimensional matched filters," *IEEE Trans. Med. Imag.*, vol. 8, no. 3, pp. 263–269, Sep. 1989.
- [27] T. Chanwimaluang and G. Fan, "An efficient algorithm for extraction of anatomical structures in retinal images," in *Proc. ICIP*, 2003, pp. 1193–1196.
- [28] M. E. Martinez-Perez, A. D. Hughes, A. V. Stanton, S. A. Thom, A. A. Bharath, and K. H. Parker, "Segmentation of retinal blood vessels based on the second directional derivative and region growing," in *Proc. ICIP*, 1999, pp. 173–176.
- [29] M. E. Martinez-Perez, A. D. Hughes, A. V. Stanton, S. A. Thom, A. A. Bharath, and K. H. Parker, "Scale-space analysis for the characterization of retinal blood vessels," in *Medical Image Computing and Computer-Assisted Intervention—MICCAI'99*, C. Taylor and A. Colchester, Eds. Springer: New York, 1999, vol. 16794, Lecture Notes Comput. Sci., pp. 90–97.
- [30] Y. Wang and S. C. Lee, "A fast method for automated detection of blood vessels in retinal images," in *IEEE Comput. Soc. Proc. Asilomar Conf.*, 1998, pp. 1700–1704.
- [31] X. Jiang and D. Mojon, "Adaptive local thresholding by verification-based multithreshold probing with application to vessel detection in retinal images," *IEEE Trans. Pattern Anal. Mach. Intell.*, vol. 254, no. 1, pp. 131–137, Jan. 2003.
- [32] F. Zana and J.-C. Klein, "Segmentation of vessel-like patterns using mathematical morphology and curvature evaluation," *IEEE Trans. Med. Imag.*, vol. 11, no. 7, pp. 1111–1119, Jul. 2001.
- [33] T. Walter and J.-C. Klein, "Segmentation of color fundus images of the human retina: Detection of the optic disc and the vascular tree using morphological techniques," in *Lecture Notes Computer Science*. Berlin: Springer-Verlag, 2001, vol. 2199, pp. 282–287.
- [34] M. Niemeijer, J. Staaf, B. van Ginneken, M. Loog, and M. D. Abràmoff, "Comparative study of retinal vessel segmentation methods on a new publicly available database," in *Proc. SPIE Med. Imag.*, M. Fitzpatrick and M. Sonka, Eds., 2004, vol. 5370, pp. 648–656.
- [35] C. Sinthanayothin, J. F. Boyce, H. L. Cook, and T. H. Williamson, "Automated localization of the optic disc, fovea, and retinal blood vessels from digital colour fundus images," *Br. J. Ophthalmol.*, vol. 83, pp. 902–911, 1999.
- [36] A. J. Frame, P. E. Undrill, J. A. Olson, K. C. McHardy, P. F. Sharp, and J. V. Forrester, "Structural analysis of retinal vessels," in *Proc. IPA*, 1997, pp. 824–827.
- [37] O. Chutatape, L. Zheng, and S. M. Krishnan, "Retinal blood vessel detection and tracking by matched Gaussian and Kalman filters," in *Proc. 20th Annu. Int. Conf. IEEE Engineering in Medicine and Biology*, 1998, pp. 3144–3149.
- [38] Y. Toliaas and S. M. Panas, "A fuzzy vessel tracking algorithm for retinal images based on fuzzy clustering," *IEEE Trans. Med. Imag.*, vol. 17, no. 2, pp. 263–273, Apr. 1998.
- [39] A. Can, H. Shen, J. N. Turner, H. L. Tanenbaum, and B. Roysam, "Rapid automated tracing and feature extraction from retinal fundus images using direct exploratory algorithms," *IEEE Trans. Inf. Technol. Biomed.*, vol. 3, no. 2, pp. 125–138, Jun. 1999.
- [40] A. M. Mendonça, A. J. Campilho, and J. R. Nunes, "Analysis of perifoveolar region in eye fundus images," in *Proc. 7th Scand. Conf. Image Anal.*, 1991, vol. 1, pp. 545–552.
- [41] W. K. Pratt, *Digital Image Processing*, 3rd ed. New York: Wiley, 2001.
- [42] T. S. Yoo, G. D. Stetten, and B. Lorensen, "Basic image processing and linear operators," in *Insight into Images*, T. S. Yoo, Ed. Wesley, MA: A. K. Peters, 2004, pp. 19–45.
- [43] P. Salembier, "Comparison of some morphological segmentation algorithms based on contrast enhancement—Application to automatic defect detection," in *Signal Process. V: Theories Appl.*, L. Torres, E. Masgrau, and M. A. Lagunas, Eds. Amsterdam, The Netherlands: Elsevier, 1990, pp. 833–836.
- [44] P. Soille, *Morphological Image Analysis: Principles and Applications*, 2nd ed. Berlin, Germany: Springer-Verlag, 2003, pp. 199–201.
- [45] M. Niemeijer and B. van Ginneken, 2002 [Online]. Available: Available: <http://www.isi.uu.nl/Research/Databases/DRIVE/results.php>
- [46] A. Hoover, STARE database [Online]. Available: Available: <http://www.ces.clemson.edu/~ahoover/stare>
- [47] J. P. M. de Sá, *Applied Statistics using SPSS, Statistica and MATLAB*. Berlin, Germany: Springer-Verlag, 2003, pp. 178–180.
- [48] D. Pavan-Langston, *Manual of ocular Diagnosis and Therapy*, 4th ed. Boston, MA: Little, Brown, 1996, p. 12.